

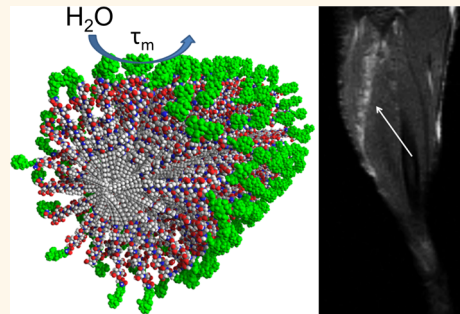
# Gd(III)-Labeled Peptide Nanofibers for Reporting on Biomaterial Localization *in Vivo*

Adam T. Preslar,<sup>†,§</sup> Giacomo Parigi,<sup>||</sup> Mark T. McClendon,<sup>†,‡</sup> Samantha S. Sefick,<sup>†</sup> Tyson J. Moyer,<sup>†</sup> Chad R. Haney,<sup>†</sup> Emily A. Waters,<sup>†</sup> Keith W. MacRenaris,<sup>§</sup> Claudio Luchinat,<sup>||</sup> Samuel I. Stupp,<sup>†,\*</sup> and Thomas J. Meade<sup>§,\*</sup>

<sup>†</sup>Departments of Chemistry, Materials Science and Engineering, and Institute for BioNanotechnology in Medicine, <sup>‡</sup>Chemical and Biological Engineering,

<sup>§</sup>Departments of Chemistry, Molecular Biosciences, Neurobiology and Radiology, and <sup>||</sup>Center for Advanced Molecular Imaging, Northwestern University, 2145 Sheridan Road, Evanston, Illinois 60208, United States and <sup>||</sup>Magnetic Resonance Center (CERM) and Department of Chemistry, University of Florence, Via Luigi Sacconi 6, 50019 Sesto Fiorentino, Italy

**ABSTRACT** Bioactive supramolecular nanostructures are of great importance in regenerative medicine and the development of novel targeted therapies. In order to use supramolecular chemistry to design such nanostructures, it is extremely important to track their fate *in vivo* through the use of molecular imaging strategies. Peptide amphiphiles (PAs) are known to generate a wide array of supramolecular nanostructures, and there is extensive literature on their use in areas such as tissue regeneration and therapies for disease. We report here on a series of PA molecules based on the well-established  $\beta$ -sheet amino acid sequence V<sub>3</sub>A<sub>3</sub> conjugated to macrocyclic Gd(III) labels for magnetic resonance imaging (MRI). These conjugates were shown to form cylindrical supramolecular assemblies using cryogenic transmission electron microscopy and small-angle X-ray scattering. Using nuclear magnetic relaxation dispersion analysis, we observed that thermal annealing of the nanostructures led to a decrease in water exchange lifetime ( $\tau_m$ ) of hundreds of nanoseconds only for molecules that self-assemble into nanofibers of high aspect ratio. We interpret this decrease to indicate more solvent exposure to the paramagnetic moiety on annealing, resulting in faster water exchange within angstroms of the macrocycle. We hypothesize that faster water exchange in the nanofiber-forming PAs arises from the dehydration and increase in packing density on annealing. Two of the self-assembling conjugates were selected for imaging PAs after intramuscular injections of the PA C<sub>16</sub>V<sub>3</sub>A<sub>3</sub>E<sub>3</sub>-NH<sub>2</sub> in the *tibialis anterior* muscle of a murine model. Needle tracts were clearly discernible with MRI at 4 days postinjection. This work establishes Gd(III) macrocycle-conjugated peptide amphiphiles as effective tracking agents for peptide amphiphile materials *in vivo* over the timescale of days.



**KEYWORDS:** self-assembly · peptide amphiphile · magnetic resonance imaging · contrast agent · biomaterials · nuclear magnetic relaxation dispersion

Supramolecular self-assembly offers biomimetic strategies to produce complex nanostructures for applications across many chemical and biological applications.<sup>1–4</sup> Self-assembly has been used to direct regeneration of tissues such as cartilage,<sup>5</sup> bone,<sup>6</sup> and blood vessels.<sup>7–10</sup> Compared to artificial systems, nanostructures based on biological building blocks have the potential advantage of biocompatibility as well as natural degradation pathways. In this context, peptide amphiphiles are useful for designing bioactive nanostructures.<sup>11</sup>

Peptide amphiphiles (PAs) that self-assemble into well-defined nanoscale

fibrous structures emulating extracellular matrices are promising in many regenerative medicine applications.<sup>12</sup> Their relatively short peptide sequences are covalently conjugated to hydrophobic fatty acid tails. The peptide sequences consist typically of charged residues for solubility and in some cases a bioactive terminus to be displayed to the biological environment. Sequences of amino acids with high  $\beta$ -sheet propensities promote assembly into one-dimensional nanostructures in water. In solution, the PAs described self-assemble into nanostructures with varying one-dimensional morphologies and physical properties that

\* Address correspondence to s-stupp@northwestern.edu, tmeade@northwestern.edu.

Received for review May 1, 2014 and accepted June 17, 2014.

Published online June 17, 2014  
10.1021/nn502393u

© 2014 American Chemical Society

depend on their specific design and assembly conditions.<sup>13–16</sup> The platform is highly versatile because it allows the incorporation of specific functions without disrupting fiber-like morphologies. Furthermore, the density of these functional structures at their termini on fiber surfaces can be controlled through coassembly with nonfunctional molecules.<sup>9,17–19</sup> Fibrous PA structures delivered to biological tissues are designed to perform their function and then biodegrade into natural building blocks. However, this degradation process, so important for understanding material function, assessing nanomaterial toxicity, and clearance, is not well understood *in vivo*. Developing MRI strategies to image PA spatiotemporal presence *in vivo* would produce a critical tool for their further development as therapies.<sup>20–22</sup>

Magnetic resonance imaging (MRI) is ideally suited to provide long-term imaging with high spatial resolution without exposing the subject to ionizing radiation. Signal intensity in MR imaging is dependent on proton relaxation rates, field strength, and acquisition sequence.<sup>23</sup> MR contrast agents accelerate magnetic relaxation to increase contrast.<sup>24,25</sup> Among  $T_1$  contrast agents, Gd(III) macrocycles have shown great clinical and research success owing to their stability and high magnetic moments.<sup>26</sup> Previously, we developed contrast agent–PA conjugates for MRI and observed that these compounds exhibited enhanced image contrast due to their slow molecular tumbling rate.<sup>27,28</sup> Recently, Ghosh *et al.* reported a series of contrast agent PAs in which the steric and electrostatic repulsions among the macrocyclic contrast agents drove changes in assembly morphology that depend on pH.<sup>29</sup>

Nuclear magnetic relaxation dispersion (NMRD) profiles, which measure proton relaxation time as a function of magnetic field strength,<sup>30</sup> provide insight into the interplay of macrocycle rotational dynamics ( $\tau_R$ ) and water exchange lifetime ( $\tau_m$ ), among other parameters.<sup>26,31–33</sup> The Florence NMRD model, developed to analyze the NMRD profiles when deviations from the Solomon–Bloembergen–Morgan (SBM) theory are expected due to the presence of ZFS, has been used to interpret the profiles by modeling water relaxation by Gd(III) macrocycles.<sup>30,34–36</sup> From these profiles, the parameters  $\tau_R$  and  $\tau_m$  can thus be extracted. With a mechanistic understanding of a contrast agent, it is possible to increase agent sensitivity through its molecular design.

We investigate here self-assembling PAs conjugated at different positions with Gd(III) contrast agents as *in vivo* implant labels and use NMRD to understand how assembly conditions affect the parameters of water relaxation, particularly  $\tau_m$ . We designed four compounds to test the effects of sterics and radial placement of the gadolinium chelate on relaxivity. A chelate based on a clinically approved agent was

chosen for its high stability.<sup>37</sup> This is particularly important when considering clinical applications and long clearance periods. PA compounds were assessed as contrast agents using relaxation measurements after dissolving in buffer, thermally annealing, and after cross-linking annealed solutions with CaCl<sub>2</sub>. Two Gd(III)–PAs were then used to fate-map implanted PA gels in the *tibialis anterior* muscle of the mouse limb over days.

## RESULTS AND DISCUSSION

Peptide amphiphiles based on the V<sub>3</sub>A<sub>3</sub> motif were chosen to promote one-dimensional assembly with strong tendency to form  $\beta$ -sheets.<sup>38</sup> Three glutamic acid residues were introduced in the peptide sequence to improve solubility and to promote strong interactions with divalent cations which can result in gel formation through charge screening. The basic PA structure explored here utilized contrast agent conjugated at the C-terminus of the peptide with (**PA1**) or without a glycine linker (**PA2**). **PA3** is similar to **PA1**, but it is conjugated with three chelates in order to investigate the potential benefits of trifunctional structures for imaging. In **PA4**, the Gd(III) contrast agent was moved closer to the fiber core while compensating for greater sterics with a stronger  $\beta$ -sheet containing one additional valine residue. Peptide amphiphiles **1–4** were synthesized using solid-phase peptide synthesis, with peptoid linkers incorporated *via* established protocols.<sup>39</sup> The peptoid residue linker provides a synthetically facile means of incorporating an alkyne functional handle. The Gd(III) macrocycle Gd(HPN<sub>3</sub>DO3A) was chosen for its chelate stability<sup>37,40,41</sup> and synthesized according to the method of Mastarone *et al.*<sup>42</sup> Gd(HPN<sub>3</sub>DO3A) was conjugated to the peptoids *via* click chemistry (Figure 1A) to afford white powders in 20% overall yield after HPLC purification (see Supporting Information Table S1 for detailed methods) and lyophilization.

Small-angle X-ray scattering (SAXS) was used to provide data regarding nanostructure size, shape, and polydispersity in solution (Figure 1B). Solutions were characterized at 1 mM in buffer after heating them to 80 °C and slowly cooling to room temperature. This procedure was used to impart ordering of filaments in solution since it was earlier found in our laboratory to promote liquid crystallinity.<sup>44</sup> As expected, the solutions became noticeably more viscous after annealing. After annealing, CaCl<sub>2</sub> was added (3.33 mM) to simulate calcium concentrations found *in vivo*. The effects of annealing followed by CaCl<sub>2</sub> addition were investigated throughout this work.

To assess SAXS profiles for structural information, fits were applied based on a core–shell cylinder form factor (see Table S3 for a list of fitted parameters). The slope of the Guiner region was approximately –1 for **PA1**, **PA2**, and **PA4**, indicating one-dimensional,

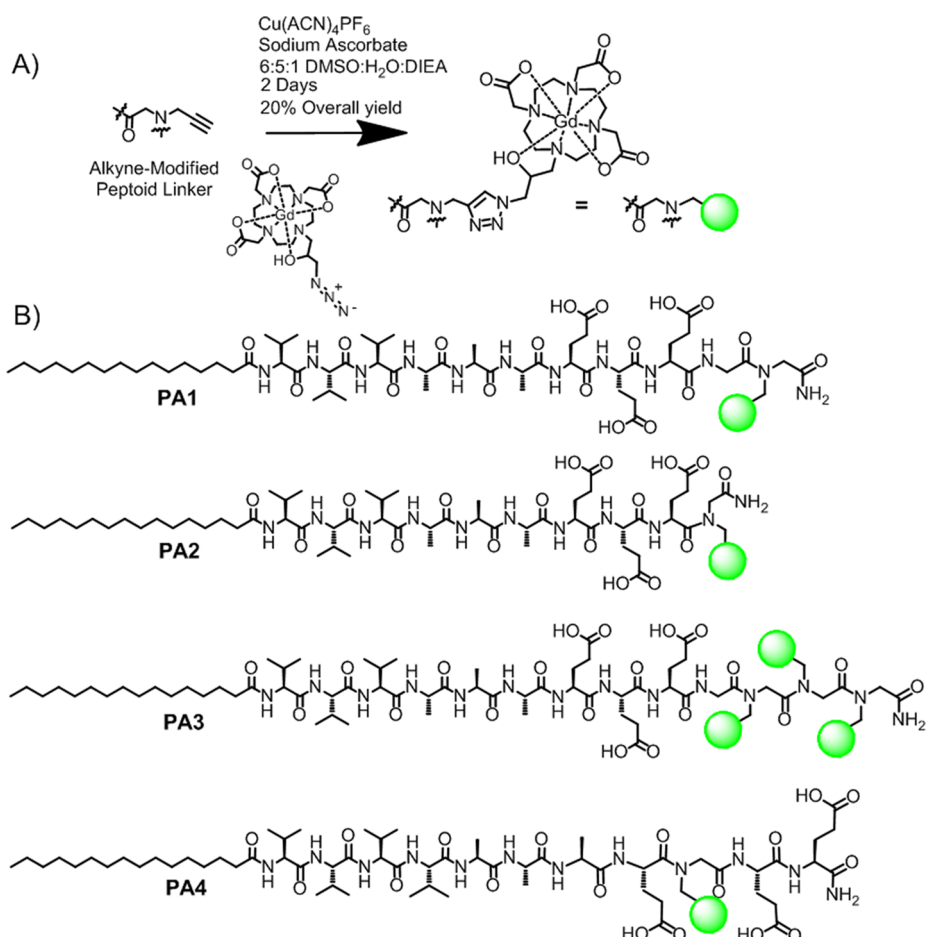


**Figure 1.** Summary of chelate conjugation chemistry and the compounds investigated in this work. (A) Click addition of azide-modified  $\text{Gd}(\text{HPN}_3\text{DO}_3\text{A})$  to the alkyne peptoid was performed in solution after cleavage from the resin. (B) Chemical structures of MR contrast agents based on conjugation of the  $\text{V}_3\text{A}_3$  peptide sequence.

high-aspect-ratio structures. In contrast, the fit of **PA3** was consistent with much shorter fibers. The scattering curve can be fit to a core–shell cylinder with very short ( $\sim 10$  nm) length. The deviation from the fit at very low  $q$  in **PA3** is likely due to aggregation for that compound. Annealing and calcium addition do not substantially change the SAXS form factors observed for **PA1–4**. However, the SAXS profile of **PA1** reveals a small shift in the scattering minimum from  $q = 0.06$  to  $q = 0.055 \text{ \AA}^{-1}$ , corresponding to a diameter change from 10.5 to 11.4 nm after thermal annealing, which suggests reorganization of the internal fiber structure. This increased radius may arise from thermal dehydration of the amino acids as the molecules adopt a more extended conformation.

Cryogenic transmission electron microscopy (cryo-TEM) was performed on all four PAs before and after thermal annealing (Figure S1 and Figure 2B, respectively). After heating to  $80^\circ\text{C}$  for 30 min and slowly cooling to room temperature, **PA1–2** fibers appeared longer (several micrometers instead of hundreds of nanometers) and were more numerous. **PA3–4** showed short fibers only a few hundred nanometers long before and after annealing. Despite an additional valine residue

to strengthen  $\beta$ -sheets in assembled **PA4**, steric repulsion among the macrocycles on adjacent molecules likely suppresses long fiber formation. These results indicate that the bulky groups should be conjugated to the outermost residue of a short PA sequence to minimize disruption of the PA nanofiber morphology and retain high-aspect-ratio structures.

Circular dichroism (CD) spectroscopy was used to determine the secondary structure of the assembled PA molecules. The CD spectra indicated strong  $\beta$ -sheet character for all the assemblies except for **PA3**, which exhibited a random coil structure (Figure S2 and Table S4). The disruption of the  $\beta$ -sheet structure in **PA3** is likely due to the steric contribution of three bulky  $\text{Gd}(\text{HP-DO}_3\text{A})$  macrocycles. **PA4** shows an intense  $\beta$ -sheet signal, as expected for a sequence with an additional valine residue due to this amino acid's high propensity to form  $\beta$ -sheets.<sup>43</sup> These CD results show a correlation between high-aspect-ratio fibers and  $\beta$ -sheet content for these conjugates.

Using a Bruker Minispec relaxometer operating at  $1.41 \text{ T}$ ,  $T_1$  and  $T_2$  relaxivity values ( $r_1$  and  $r_2$ ) were determined for each agent (Table 1, measurements detailed in Figures S3–S10 and Tables S5–S12). At higher

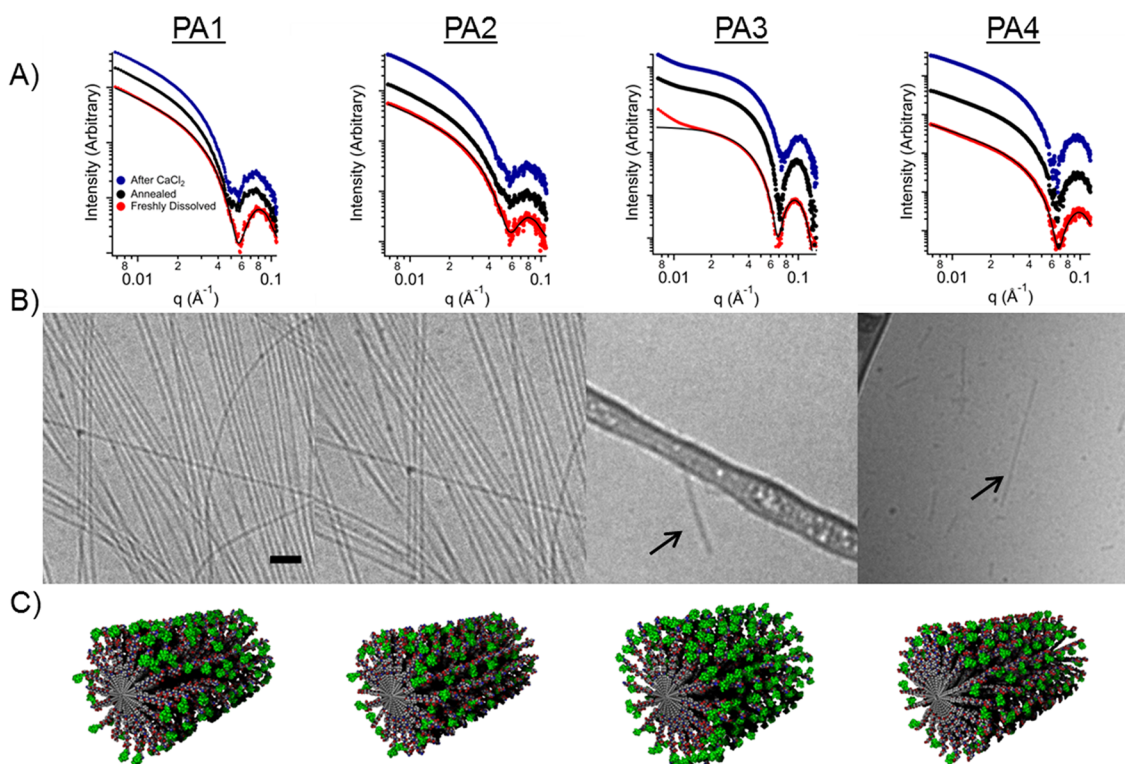


**Figure 2.** (A) Small-angle X-ray scattering data for each PA when dissolved in 10 mM Tris buffer (red), after thermal annealing (black), and after the addition of  $\text{CaCl}_2$  to thermally annealed solutions (blue). Profile fits (black) are applied for the buffered case only. (B) Cryo-TEM of the same conjugates after thermal annealing (scale bar is 200 nm). (C) Molecular graphics representation of the various peptide amphiphile assemblies. Gadolinium macrocycles are shown in green.

**TABLE 1. Summary of PA  $T_1$  and  $T_2$  Relaxivities as a Function of Condition<sup>a</sup>**

	$\text{H}_2\text{O}$		Tris buffer (pH 7.4)		after thermal annealing		addition of $\text{CaCl}_2$	
	$r_1$	$r_2$	$r_1$	$r_2$	$r_1$	$r_2$	$r_1$	$r_2$
<b>PA1</b>	$16.5 \pm 0.5$	$34 \pm 1$	$16 \pm 2$	$30 \pm 4$	$19.0 \pm 0.6$	$37 \pm 1$	$18.4 \pm 0.2$	$40.0 \pm 0.1$
<b>PA2</b>	$17.3 \pm 0.8$	$39 \pm 2$	$16.7 \pm 0.2$	$32.2 \pm 0.5$	$16.9 \pm 0.2$	$28.6 \pm 0.6$	$21.7 \pm 0.1$	$45 \pm 2$
<b>PA3</b>	$16.4 \pm 0.6$	$30 \pm 2$	$15.8 \pm 0.5$	$25.3 \pm 0.2$	$16.4 \pm 0.6$	$25.2 \pm 0.2$	$16.5 \pm 0.8$	$25 \pm 1$
<b>PA4</b>	$17 \pm 1$	$31 \pm 2$	$15.6 \pm 0.1$	$25.3 \pm 0.2$	$16.0 \pm 0.1$	$25.2 \pm 0.2$	$18 \pm 1$	$25 \pm 1$

<sup>a</sup> All measurements were obtained at 1.41 T and are measured in  $\text{mM}^{-1} \text{s}^{-1}$ .

concentrations and long repetition times,  $T_2$  relaxation is expected to dominate, generating negative contrast. At lower concentrations and short repetition times,  $T_1$  relaxation is more likely to dominate, generating positive contrast.  $T_1$  relaxivity of all supramolecular nanostructures shows substantial improvement when compared to commercial agents ( $r_1 \sim 4 \text{ mM}^{-1} \text{ s}^{-1}$ ). These results show that **PA1–4** are potentially useful for labeling PA implants for fate-mapping. Interestingly, thermal annealing followed by addition of  $\text{CaCl}_2$  caused complex changes in the observed agent relaxivity (Table 1). **PA1** showed an increase in relaxivity upon thermal annealing, as expected for a macrocycle more accessible to bulk solvent. This increased accessibility is consistent with a more extended molecular structure as indicated by SAXS. In contrast, **PA2** shows no change in relaxivity with annealing, but relaxivity increases upon  $\text{CaCl}_2$  addition to the annealed

solutions. **PA3–4**, which did not produce high-aspect-ratio fibers, showed little change in relaxivity when annealed or when  $\text{Ca}^{2+}$  ions were added for charge screening (possibly electrostatic binding among nanofibers). Based on these results, increased relaxivity on annealing is expected for peptide amphiphiles exhibiting  $\beta$ -sheet character that generate high-aspect-ratio fiber nanostructures.

In order to establish which parameter was dominant in relaxivity changes, NMRD profiles of each PA were measured. NMRD profiles for all four PAs at 25 and 37 °C are shown in Figure 3 and Figures S11–S16 with parameter fits obtained using the “modified Florence” approach.<sup>44–46</sup> In the fits, a Lipari-Szabo order parameter  $S^2$  was included to consider the effect of local motions which may superimpose to the global motion of the nanostructures. A smaller  $S^2$  value indicates a less restricted local mobility (*i.e.*, a more flexible linkage

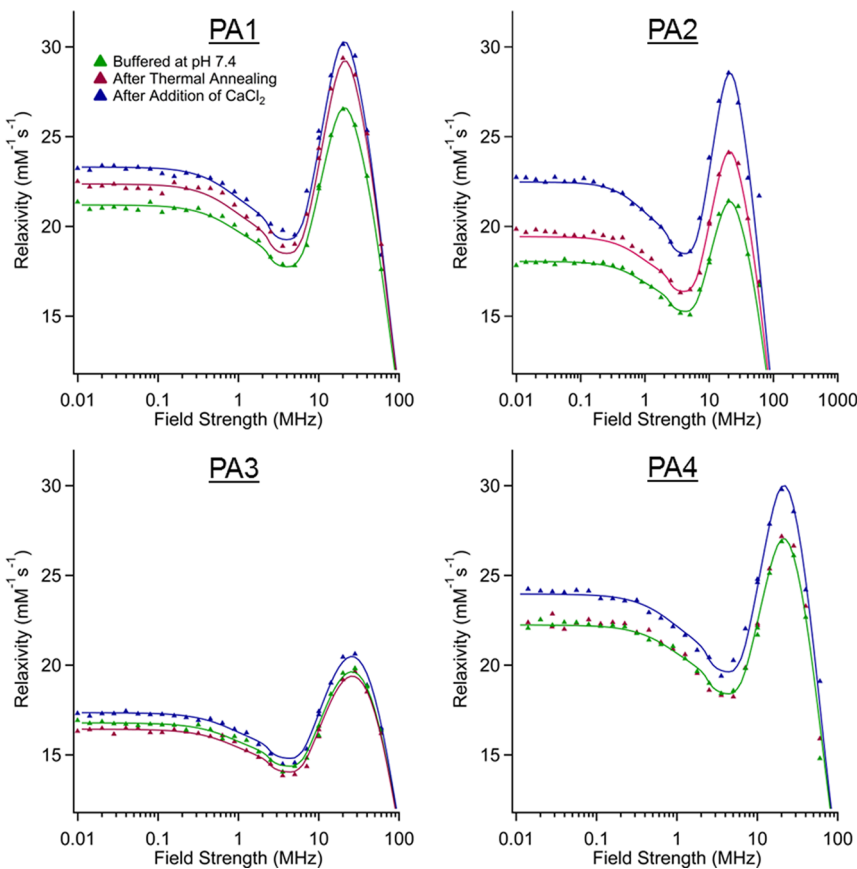


**Figure 3.** NMRD profiles for all PAs at three different conditions. All profiles were collected at 37 °C with a PA concentration of 2 mM. The fits for PA4 in annealed and buffered conditions are identical.

**TABLE 2. Summary of Best-Fit Values of Key Parameters Obtained from Data Fits at 37 °C**

	$\tau_m$ (ns)				
	buffered	annealed	$\text{Ca}^{2+}$	$S^2$	$\tau_{\text{local}}$ (ns)
PA1	465	400	380	0.25	4
PA2	640	540	410	0.3	4
PA3	690	700	650	0.0	4
PA4	480	480	420	0.25	5.5

between fiber and macrocycle). **PA3** shows a substantially larger local motional freedom, consistent with its random coil secondary structure. The NMRD fits show  $\tau_m$  is primarily responsible for the variation in relaxivity observed upon annealing and  $\text{Ca}(\text{II})$  cross-linking (Table 2). We believe that annealing and calcium addition change macrocycle presentation on the fiber surface, likely extending them from the structure with increased peptide packing density and facilitating faster water exchange. This effect is heavily structure-dependent and is even observed differently based on the inclusion of a glycine linker (**PA2**) compared to without (**PA1**). The same changes in  $\tau_m$  are not observed for PAs that do not form high-aspect-ratio assemblies (**PA3–4**), implying that the packing of the **PA1–2** assemblies is key to this  $\tau_m$  effect.

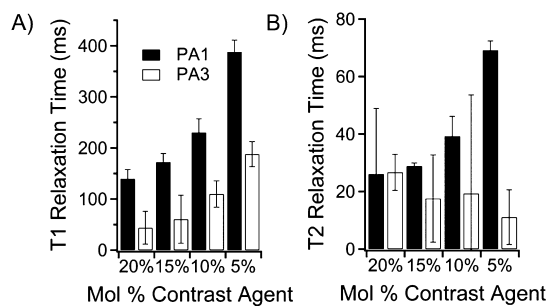


**Figure 4.** Relaxation time measurements of PA solutions for PA1 and PA3 in Tris buffer at 7 T. (A) Summary of  $T_1$  values of mixtures of PA1 and PA3 with the filler sequence  $\text{C}_{16}\text{V}_3\text{A}_3\text{E}_3\text{-NH}_2$ . (B) Summary of  $T_2$  values of mixtures of PA1 and PA3 with the filler sequence  $\text{C}_{16}\text{V}_3\text{A}_3\text{E}_3\text{-NH}_2$ . The short  $T_2$  for PA3 confirms that  $T_2$  relaxation is likely dominating  $T_1$  relaxation of PA3.

**PA1** produced high-aspect-ratio nanostructures, and **PA3**, with its three appended contrast agents, did not form high-aspect-ratio nanostructures. These two PAs were chosen for testing to follow *in vivo* degradation. To determine optimum contrast agent loading, **PA1** and **PA3** were mixed in varied ratios with  $\text{C}_{16}\text{V}_3\text{A}_3\text{E}_3\text{-NH}_2$  PA. The total concentration of unlabeled PA and  $\text{Gd}(\text{III})\text{-PA}$  was kept constant at 1.3 mM, and measurements were obtained using  $T_1$  and  $T_2$  mapping sequences at 7 T.  $T_1$  showed an inverse relationship versus gadolinium concentration, as expected

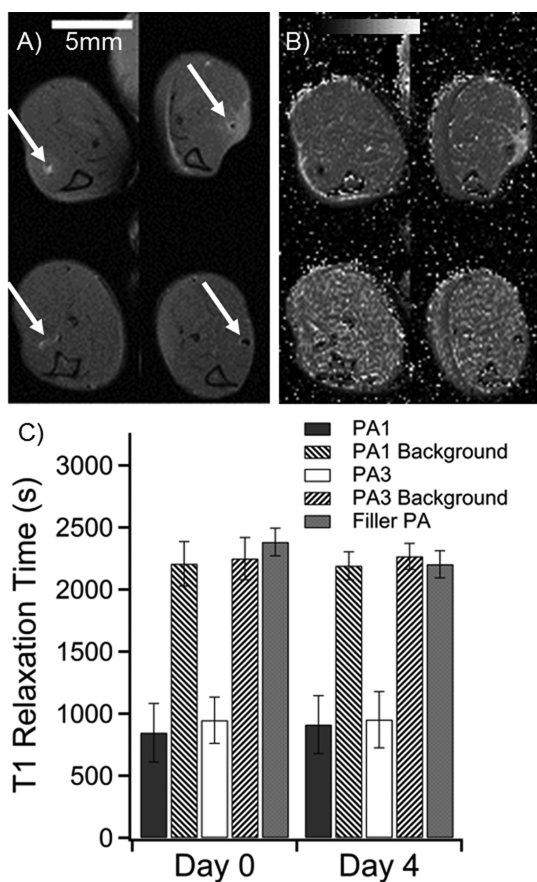


**Figure 5. Summary of *in vivo* measurements of PA1 and PA3 in a murine leg model.** (A) Anatomical scan of mouse legs immediately after injection (top row) and after 4 days (bottom row). The PA injections are indicated by white arrows. PA1 produces positive contrast in white (left column), while PA3 produces negative contrast (right column). (B)  $T_1$  maps of the same mouse at the same image positions as in A. Dark areas represent regions with very short  $T_1$  times. (C) Averaged image  $T_1$  times from regions of interest for all mice at all slices where PA was visible. Filler (unlabeled) PA was not visible (Figure S27). Filler PA  $T_1$  was measured as a best approximation for PA position based on the injection location. Background was measured by averaging  $T_1$  values of muscle tissue several millimeters from the PA injection.

for a homogeneous agent in solution (Figure 4A).<sup>47</sup> This suggests that relaxivity is independent of Gd(III)–PA to unlabeled PA ratio. At 10 mol % of PA,  $T_1$  relaxation time was sufficiently fast (100–250 ms for both conjugates) to generate large contrast. Figure 4B shows the  $T_2$  relaxation time of the same solutions.  $T_2$  shortening reduces image contrast at higher Gd(III)–PA loadings.

To measure degradation *in vivo*, six wild-type mice received approximately 4  $\mu$ L injections of PA gels at 1 wt % loaded with 10 mol % of Gd(III)–PA relative to

$C_{16}V_3A_3E_3-NH_2$ . The injections were applied with a modified syringe pump designed to inject while withdrawing the needle to produce a gelled track of PA in the *tibialis anterior*. Injection volume varied (Table S13) because track length varied slightly with mouse size and small variations in each injection geometry. The tract geometry was chosen to give accurate  $T_1$  determinations because imaging slice thickness could be greater without volume averaging effects. A total of five legs were injected with **PA1**, four legs with **PA3**, and three with 100%  $C_{16}V_3A_3E_3-NH_2$  as a control. Mice were imaged at day 0 immediately after injections and again at day 4. The Gd(III)–PA was clearly visible in all cases, while the 100%  $C_{16}V_3A_3E_3-NH_2$  control produced no contrast enhancement (Figures 5 and S27–S29). **PA1** produced  $T_1$ -weighted positive contrast, while **PA3** produced  $T_2$ -weighted negative contrast. After day 4, the mice were sacrificed and the leg muscles were subjected to ICP-MS analysis to measure Gd(III) retention. ICP-MS revealed that  $62 \pm 8\%$  of **PA1** and  $54 \pm 9\%$  of **PA3** remained in the mouse leg after 4 days (Table S13). The  $T_1$  relaxation time of regions of interest did not appreciably change after 4 days, as shown in Figure 5C. Stable  $T_1$  times indicate that PA concentration did not change substantially over the 4 day period. These ICP-MS and  $T_1$  map results show that Gd(III)–PAs are a promising means of following PA gel biodegradation over time.

## CONCLUSIONS

We have developed supramolecular MRI contrast agent–peptide amphiphile conjugates that investigate the relationship between nanostructure morphology and MR contrast agent relaxivity. **PA1–4** all showed high,  $\tau_R$ -modulated, relaxivity with optimum compounds and conditions producing relaxivities greater than  $20 \text{ mM}^{-1} \text{ s}^{-1}$  at 60 MHz. Thermal annealing and the presence of Ca(II) ions in solution increased relaxivity of conjugates that formed long fibers. These changes are a result of water exchange lifetime shortening, providing a new route to controlling water exchange on the surface of contrast agent nanostructures. We show that annealing, cross-linking with Ca(II), and even the inclusion of a single glycine linker can effect  $\tau_m$ . Gd(III)–PA complexes were used to fate-map a PA gel in an *in vivo* mouse model, showing persistence over a 4 day period. The supramolecular structures formed by self-assembly of these Gd(III)–PAs provide a useful approach to track the fate of biomaterials over time after they have been implanted *in vivo*.

## METHODS

$^1\text{H}$  NMRD profiles were collected with a Stelar Spinmaster FFC-2000-1T fast field cycling relaxometer in the 0.01–40 MHz proton Larmor frequency range, at 293 and 310 K. Longitudinal

relaxation rates were measured with an error smaller than 1%. Proton relaxivities were calculated by subtracting the diamagnetic contribution of the peptide nanofibers in the absence of Gd(III) from the relaxation rates of the paramagnetic samples

and normalizing to 1 mM Gd(III) concentration. The profiles were analyzed using the Freed model for outer-sphere relaxation<sup>48,49</sup> and the modified Florence NMRD program for the inner-sphere relaxation.<sup>45,46,50</sup> The effect of static ZFS on nuclear relaxation is considered along with transient ZFS, where modulation is responsible for electron relaxation, provided molecular reorientation time is much longer than electron relaxation time.<sup>51,52</sup> NMRD data and fits are provided in the Supporting Information (Figures S11–S16).

C57BL/6N, wild-type mice were obtained from Charles River. A 21 gauge needle was used to inject annealed Gd(III)-PA solutions into the *tibialis anterior* muscle of each leg of each mouse. Approximately 4.5  $\mu$ L was injected at a rate of 5  $\mu$ L/min, while retracting the needle at a rate of 1 cm/min. This injection method allows for the PA solution to be introduced at a very slow rate, so that gelation may occur by *in vivo* divalent ions inside the needle tract. The injection and retraction was done using a modified NE-300 Just Infusion Syringe Pump (Figure S25). All animal studies were conducted at Northwestern University in accordance with the National Institutes of Health Guide for the Care and Use of Laboratory Animals and established institutional animal use and care protocols.

All images were acquired on a Bruker 7T Pharmascan MRI system using a 38 mm quadrature coil. Anatomical images were acquired with a fat-saturated multispin multiecho (MSME) pulse sequence ( $T_R/T_E = 800$  ms/11.5 ms) with 5 slices of 1 mm thickness and two signal averages. The field of view was 4  $\times$  4 cm with a 300  $\times$  300 pixel matrix size.  $T_1$  maps for the animal experiments were acquired using a rapid acquisition with relaxation enhancement (RARE)-based  $T_1$  map protocol with repetition times 157, 200, 400, 800, 1200, 3000, and 4000 ms with one average and no fat saturation.  $T_2$  acquisitions were taken using a fat-saturated MSME  $T_2$  map sequence with repetition time 4000 ms and echo times 11.6, 23.3, 34.9, 46.5, 58.2, 69.8, 81.4, 93.1, 104.7, and 116.4 ms. Slice geometry parameters for  $T_1$  and  $T_2$  maps were the same as above.  $T_1$  maps were generated with a saturation-recovery fit for each pixel using the Jim software package (Xinapse Systems, Colchester, UK). All images used as data in this work are provided in the Supporting Information (Figures S27–S29).

**Conflict of Interest:** The authors declare no competing financial interest.

**Acknowledgment.** The authors gratefully acknowledge funding from National Institutes of Health's (NIH) National Heart, Lung and Blood Institute, under award P01HL108795, the National Institute of Biomedical Imaging and Engineering, under award EB005866, and the National Cancer Institute Center for Cancer Nanotechnology Excellence initiative at Northwestern University Award No. U54CA151880. NMRD work was supported by the Ente Cassa di Risparmio di Firenze, and the European Commission contract Bio-NMR No. 261863. The Center for Advanced Molecular Imaging (CAMI) and the Quantitative Bioelemental Imaging Center (QBIC) at Northwestern provided instrumentation for *in vivo* studies. Compound purification and characterization was performed at the Institute for BioNanotechnology in Medicine (IBNAM) and the Integrated Molecular Structure Education and Research Center (IMSERC). The Biological Imaging Facility (BIF) and Keck Biophysics facilities at Northwestern, Magnetic Resonance Center (CERM) at the University of Florence, provided further instrumentation used in this work. Argonne National Lab's Advanced Photon Source (APS) Synchrotron was used to acquire small-angle X-ray scatter data. APS operates under the Department of Energy's Office of Science as a user facility. SAXS experiments were carried out at the DuPont–Northwestern–Dow Collaborative Access Team (DND-CAT). DND-CAT is located at sector 5 of the APS and is a joint venture between The Dow Chemical Company, Northwestern University, and E.I. DuPont de Nemours & Company. Use of the Advanced Photon Source, an Office of Science User Facility operated for the U.S. Department of Energy (DOE) Office of Science by Argonne National Laboratory, was supported by the U.S. DOE under Contract No. DE-AC02-06CH11357. M. Allegrozzi (University of Florence) is acknowledged for NMRD sample preparation, S. Weigand

(Argonne National Laboratory) for SAXS assistance, L. Palmer for helpful discussions, and M. Seniw for the preparation of graphics.

**Supporting Information Available:** Details of synthesis, purification, chemical characterization, NMRD fitting procedure, additional TEM images, relaxometry measurements, *in vivo* ICP-MS, and all MR images acquired are available. This material is available free of charge via the Internet at <http://pubs.acs.org>.

## REFERENCES AND NOTES

- Stupp, S. I.; Palmer, L. C. Supramolecular Chemistry and Self-Assembly in Organic Materials Design. *Chem. Mater.* **2013**, *26*, 507–518.
- Webber, M. J.; Berns, E. J.; Stupp, S. I. Supramolecular Nanofibers of Peptide Amphiphiles for Medicine. *Isr. J. Chem.* **2013**, *53*, 530–554.
- Palmer, L. C.; Stupp, S. I. Molecular Self-Assembly into One-Dimensional Nanostructures. *Acc. Chem. Res.* **2008**, *41*, 1674–1684.
- Aida, T.; Meijer, E. W.; Stupp, S. I. Functional Supramolecular Polymers. *Science* **2012**, *335*, 813–817.
- Shah, R. N.; Shah, N. A.; Del Rosario Lim, M. M.; Hsieh, C.; Nuber, G.; Stupp, S. I. Supramolecular Design of Self-Assembling Nanofibers for Cartilage Regeneration. *Proc. Natl. Acad. Sci. U.S.A.* **2010**, *107*, 3293–3298.
- Lee, S. S.; Huang, B. J.; Kaltz, S. R.; Sur, S.; Newcomb, C. J.; Stock, S. R.; Shah, R. N.; Stupp, S. I. Bone Regeneration with Low Dose BMP-2 Amplified by Biomimetic Supramolecular Nanofibers within Collagen Scaffolds. *Biomaterials* **2012**, *33*, 452–459.
- Webber, M. J.; Tongers, J.; Newcomb, C. J.; Marquardt, K. T.; Bauersachs, J.; Losordo, D. W.; Stupp, S. I. Supramolecular Nanostructures that Mimic VEGF as a Strategy for Ischemic Tissue Repair. *Proc. Natl. Acad. Sci. U.S.A.* **2011**, *108*, 13438–13443.
- Webber, M. J.; Han, X. Q.; Murthy, S. N. P.; Rajangam, K.; Stupp, S. I.; Lomasney, J. W. Capturing the Stem Cell Paracrine Effect Using Heparin-Presenting Nanofibres To Treat Cardiovascular Diseases. *J. Tissue Eng. Regener. Med.* **2010**, *4*, 600–610.
- Silva, G. A.; Czeisler, C.; Niece, K. L.; Beniash, E.; Harrington, D. A.; Kessler, J. A.; Stupp, S. I. Selective Differentiation of Neural Progenitor Cells by High-Epitope Density Nanofibers. *Science* **2004**, *303*, 1352–1355.
- Beniash, E.; Hartgerink, J. D.; Storrie, H.; Stendahl, J. C.; Stupp, S. I. Self-Assembling Peptide Amphiphile Nanofiber Matrices for Cell Entrapment. *Acta Biomater.* **2005**, *1*, 387–397.
- Hartgerink, J. D.; Beniash, E.; Stupp, S. I. Self-Assembly and Mineralization of Peptide-Amphiphile Nanofibers. *Science* **2001**, *294*, 1684–1688.
- Webber, M. J.; Kessler, J. A.; Stupp, S. I. Emerging Peptide Nanomedicine to Regenerate Tissues and Organs. *J. Int. Med.* **2010**, *267*, 71–88.
- Pashuck, E. T.; Cui, H. G.; Stupp, S. I. Tuning Supramolecular Rigidity of Peptide Fibers through Molecular Structure. *J. Am. Chem. Soc.* **2010**, *132*, 6041–6046.
- Pashuck, E. T.; Stupp, S. I. Direct Observation of Morphological Transformation from Twisted Ribbons into Helical Ribbons. *J. Am. Chem. Soc.* **2010**, *132*, 8819–8821.
- Zhang, S. M.; Greenfield, M. A.; Mata, A.; Palmer, L. C.; Bitton, R.; Mantei, J. R.; Aparicio, C.; de la Cruz, M. O.; Stupp, S. I. A Self-Assembly Pathway to Aligned Monodomain Gels. *Nat. Mater.* **2010**, *9*, 594–601.
- Ortony, J. H.; Newcomb, C. J.; Matson, J. B.; Palmer, L. C.; Doan, P. E.; Hoffman, B. M.; Stupp, S. I. Internal Dynamics of a Supramolecular Nanofiber. *Nat. Mater.* **2014**, *10*.1038/nmat3979.
- Shah, R. N.; Shah, N. A.; Lim, M. M. D.; Hsieh, C.; Nuber, G.; Stupp, S. I. Supramolecular Design of Self-Assembling Nanofibers for Cartilage Regeneration. *Proc. Natl. Acad. Sci. U.S.A.* **2010**, *107*, 3293–3298.

18. Storrie, H.; Guler, M. O.; Abu-Amara, S. N.; Volberg, T.; Rao, M.; Geiger, B.; Stupp, S. I. Supramolecular Crafting of Cell Adhesion. *Biomaterials* **2007**, *28*, 4608–4618.
19. Webber, M. J.; Tongers, J.; Renault, M. A.; Roncalli, J. G.; Losordo, D. W.; Stupp, S. I. Development of Bioactive Peptide Amphiphiles for Therapeutic Cell Delivery. *Acta Biomater.* **2010**, *6*, 3–11.
20. Appel, A. A.; Anastasio, M. A.; Larson, J. C.; Brey, E. M. Imaging Challenges in Biomaterials and Tissue Engineering. *Biomaterials* **2013**, *34*, 6615–6630.
21. Karfeld-Sulzer, L. S.; Waters, E. A.; Davis, N. E.; Meade, T. J.; Barron, A. E. Multivalent Protein Polymer MRI Contrast Agents: Controlling Relaxivity via Modulation of Amino Acid Sequence. *Biomacromolecules* **2010**, *11*, 1429–1436.
22. Karfeld-Sulzer, L. S.; Waters, E. A.; Kohlmeir, E. K.; Kissler, H.; Zhang, X.; Kaufman, D. B.; Barron, A. E.; Meade, T. J. Protein Polymer MRI Contrast Agents: Longitudinal Analysis of Biomaterials *In Vivo*. *Magn. Reson. Med.* **2011**, *65*, 220–228.
23. Frullano, L.; Meade, T. Multimodal MRI Contrast Agents. *JBIC, J. Biol. Inorg. Chem.* **2007**, *12*, 939–949.
24. Hung, A. H.; Duch, M. C.; Parigi, G.; Rotz, M. W.; Manus, L. M.; Mastarone, D. J.; Dam, K. T.; Gits, C. C.; MacRenaris, K. W.; Luchinat, C.; Hersam, M. C.; Meade, T. J. Mechanisms of Gadographene-Mediated Proton Spin Relaxation. *J. Phys. Chem. C* **2013**, *117*, 16263–16273.
25. Matosziuk, L. M.; Leibowitz, J. H.; Heffern, M. C.; MacRenaris, K. W.; Ratner, M. A.; Meade, T. J. Structural Optimization of Zn(II)-Activated Magnetic Resonance Imaging Probes. *Inorg. Chem.* **2013**, *52*, 12250–12261.
26. Caravan, P.; Ellison, J. J.; McMurry, T. J.; Lauffer, R. B. Gadolinium(III) Chelates as MRI Contrast Agents: Structure, Dynamics, and Applications. *Chem. Rev.* **1999**, *99*, 2293–2352.
27. Bull, S. R.; Guler, M. O.; Bras, R. E.; Venkatasubramanian, P. N.; Stupp, S. I.; Meade, T. J. Magnetic Resonance Imaging of Self-Assembled Biomaterial Scaffolds. *Bioconjugate Chem.* **2005**, *16*, 1343–1348.
28. Bull, S. R.; Guler, M. O.; Bras, R. E.; Meade, T. J.; Stupp, S. I. Self-Assembled Peptide Amphiphile Nanofibers Conjugated to MRI Contrast Agents. *Nano Lett.* **2005**, *5*, 1–4.
29. Ghosh, A.; Haverick, M.; Stump, K.; Yang, X.; Tweedle, M. F.; Goldberger, J. E. Fine-Tuning the pH Trigger of Self-Assembly. *J. Am. Chem. Soc.* **2012**, *134*, 3647–3650.
30. Caravan, P.; Parigi, G.; Chasse, J. M.; Cloutier, N. J.; Ellison, J. J.; Lauffer, R. B.; Luchinat, C.; McDermid, S. A.; Spiller, M.; McMurry, T. J. Albumin Binding, Relaxivity, and Water Exchange Kinetics of the Diastereoisomers of Ms-325, a Gadolinium(III)-Based Magnetic Resonance Angiography Contrast Agent. *Inorg. Chem.* **2007**, *46*, 6632–6639.
31. Zech, S. G.; Sun, W. C.; Jacques, V.; Caravan, P.; Astashkin, A. V.; Raitsimring, A. M. Probing the Water Coordination of Protein-Targeted MRI Contrast Agents by Pulsed Endor Spectroscopy. *ChemPhysChem* **2005**, *6*, 2570–2577.
32. Zech, S. G.; Eldredge, H. B.; Lowe, M. P.; Caravan, P. Protein Binding to Lanthanide(III) Complexes Can Reduce the Water Exchange Rate at the Lanthanide. *Inorg. Chem.* **2007**, *46*, 3576–3584.
33. Manus, L. M.; Mastarone, D. J.; Waters, E. A.; Zhang, X. Q.; Schultz-Sikma, E. A.; MacRenaris, K. W.; Ho, D.; Meade, T. J. Gd(III)-Nanodiamond Conjugates for MRI Contrast Enhancement. *Nano Lett.* **2010**, *10*, 484–489.
34. Major, J. L.; Parigi, G.; Luchinat, C.; Meade, T. J. The Synthesis and *In Vitro* Testing of a Zinc-Activated MRI Contrast Agent. *Proc. Natl. Acad. Sci. U.S.A.* **2007**, *104*, 13881–13886.
35. Li, W. H.; Parigi, G.; Fragai, M.; Luchinat, C.; Meade, T. J. Mechanistic Studies of a Calcium-Dependent MRI Contrast Agent. *Inorg. Chem.* **2002**, *41*, 4018–4024.
36. Song, Y.; Xu, X.; MacRenaris, K. W.; Zhang, X. Q.; Mirkin, C. A.; Meade, T. J. Multimodal Gadolinium-Enriched DNA-Gold Nanoparticle Conjugates for Cellular Imaging. *Angew. Chem., Int. Ed.* **2009**, *48*, 9143–9147.
37. Tweedle, M. F. The Prohance Story: The Making of a Novel MRI Contrast Agent. *Eur. Radiol.* **1997**, *7*, S225–S230.
38. Newcomb, C. J.; Sur, S.; Ortony, J. H.; Lee, O.-S.; Matson, J. B.; Boekhoven, J.; Yu, J. M.; Schatz, G. C.; Stupp, S. I. Cell Death versus Cell Survival Instructed by Supramolecular Cohesion of Nanostructures. *Nat. Commun.* **2014**, *5*, 3321.
39. Nam, K. T.; Shelby, S. A.; Choi, P. H.; Marciel, A. B.; Chen, R.; Tan, L.; Chu, T. K.; Mesch, R. A.; Lee, B. C.; Connolly, M. D.; Kisielowski, C.; Zuckermann, R. N. Free-Floating Ultrathin Two-Dimensional Crystals from Sequence-Specific Peptoid Polymers. *Nat. Mater.* **2010**, *9*, 454–460.
40. Kirchin, M. A.; Runge, V. M. Contrast Agents for Magnetic Resonance Imaging: Safety Update. *Top. Magn. Reson. Imaging* **2003**, *14*, 426–435.
41. Tweedle, M. F.; Hagan, J. J.; Kumar, K.; Mantha, S.; Chang, C. A. Reaction of Gadolinium Chelates with Endogenously Available Ions. *Magn. Reson. Imaging* **1991**, *9*, 409–415.
42. Mastarone, D. J.; Harrison, V. S.; Eckermann, A. L.; Parigi, G.; Luchinat, C.; Meade, T. J. A Modular System for the Synthesis of Multiplexed Magnetic Resonance Probes. *J. Am. Chem. Soc.* **2011**, *133*, 5329–5337.
43. Minor, D. L.; Kim, P. S. Measurement of the  $\beta$ -Sheet-Forming Propensities of Amino Acids. *Nature* **1994**, *367*, 660–663.
44. Bertini, I.; Galas, O.; Luchinat, C.; Messori, L.; Parigi, G. A Theoretical-Analysis of the H-1 Nuclear Magnetic-Relaxation Dispersion Profiles of Diferric Transferrin. *J. Phys. Chem.* **1995**, *99*, 14217–14222.
45. Bertini, I.; Kowalewski, J.; Luchinat, C.; Nilsson, T.; Parigi, G. Nuclear Spin Relaxation in Paramagnetic Complexes of  $S = 1$ : Electron Spin Relaxation Effects. *J. Chem. Phys.* **1999**, *111*, 5795–5807.
46. Kruk, D.; Nilsson, T.; Kowalewski, J. Nuclear Spin Relaxation in Paramagnetic Systems with Zero-Field Splitting and Arbitrary Electron Spin. *Phys. Chem. Chem. Phys.* **2001**, *3*, 4907–4917.
47. Merbach, A. E. *The Chemistry of Contrast Agents in Medical Magnetic Resonance Imaging*; Wiley: Chichester, UK, 2001.
48. Hwang, L.-P.; Freed, J. H. Dynamic Effects of Pair Correlation Functions on Spin Relaxation by Translational Diffusion in Liquids. *J. Chem. Phys.* **1975**, *63*, 4017–4025.
49. Polnaszek, C. F.; Bryant, R. G. Nitroxide Radical Induced Solvent Proton Relaxation: Measurement of Localized Translational Diffusion. *J. Chem. Phys.* **1984**, *81*, 4038–4045.
50. Bertini, I.; Galas, O.; Luchinat, C.; Parigi, G. Computer-Program for the Calculation of Paramagnetic Enhancements Nuclear-Relaxation Rates in Slowly Rotating Systems. *J. Magn. Reson., Ser. A* **1995**, *113*, 151–158.
51. Kowalewski, J.; Kruk, D.; Parigi, G. NMR Relaxation in Solution of Paramagnetic Complexes: Recent Theoretical Progress for  $S \geq 1$ . *Adv. Inorg. Chem.* **2005**, *57*, 41–104.
52. Kowalewski, J.; Luchinat, C.; Nilsson, T.; Parigi, G. Nuclear Spin Relaxation in Paramagnetic Systems: Electron Spin Relaxation Effects under Near-Redfield Limit Conditions and Beyond. *J. Phys. Chem. A* **2002**, *106*, 7376–7382.